Supporting information for

Spectroscopic and reactivity comparisons between nonheme oxoiron(IV) and oxoiron(V) species bearing the same ancillary ligand

Valeria Dantignana,[a] Joan Serrano-Plana,[a] Apparao Draksharapu,[b] Carla Magallón,[a] Saikat Banerjee,[b] Ruixi Fan,[c] Ilaria Gamba,[a] Yisong Guo,[c] Lawrence Que Jr.,[b] Miquel Costas,[a] Anna Company[a]

[a] V. Dantignana, J. Serrano-Plana, C. Magallón, I. Gamba, A. Company, M. Costas
Institut de Química Computacional i Catàlisi (IQCC), Departament de Química, Universitat de Girona. C/ M. Aurèlia Capmany 69, 17003 Girona (Catalonia, Spain). E-mail: anna.company@udg.edu, miquel.costas@udg.edu

[b] A. Draksharapu, S. Banerjee, L. Que Jr.
Department of Chemistry and Center for Metals in Biocatalysis, University of Minnesota, Minneapolis, MN 55455 (United States). E-mail: larryque@umn.edu

[c] R. Fan, Y. Guo
Department of Chemistry, Carnegie Mellon University, 4400 Fifth Avenue, Pittsburgh, Pennsylvania 15213 (USA)

Table of contents

1. Characterization of d_4-PyNMe$_3$, d_4-1·CF$_3$SO$_3$ and 1·SbF$_6$

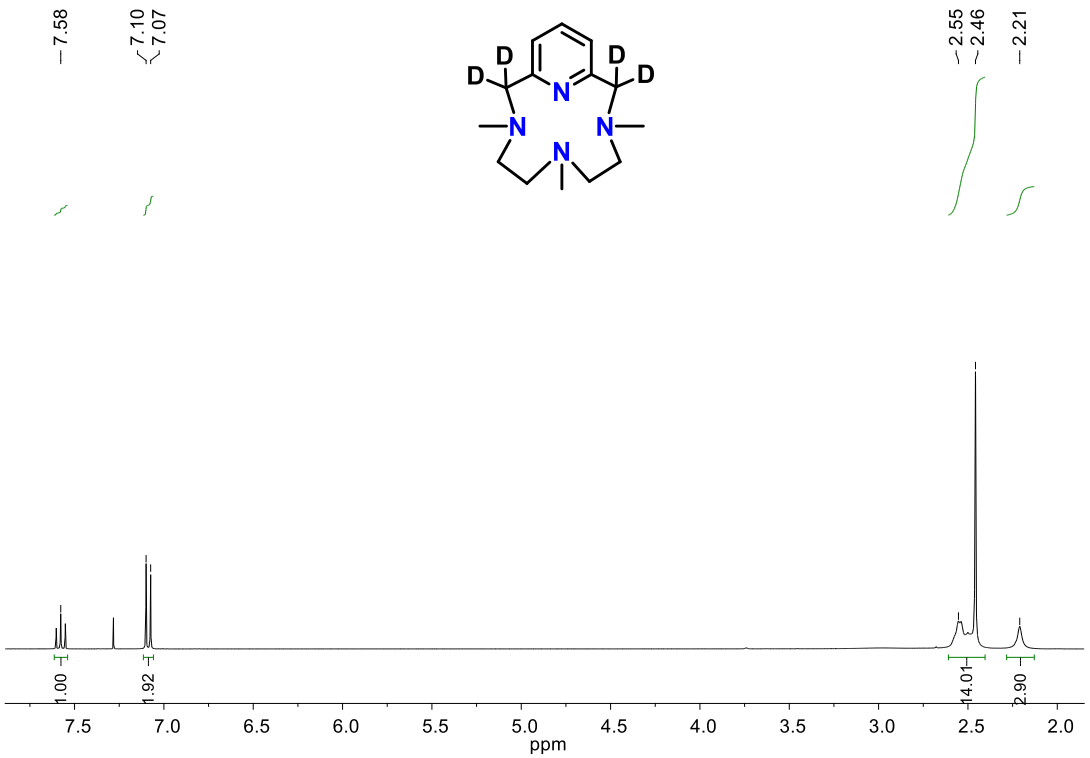

Figure S1. ^{1}H-NMR spectrum of **d_4-PyNMe$_3$** in $CDCl_3$ at 298 K (400 MHz).

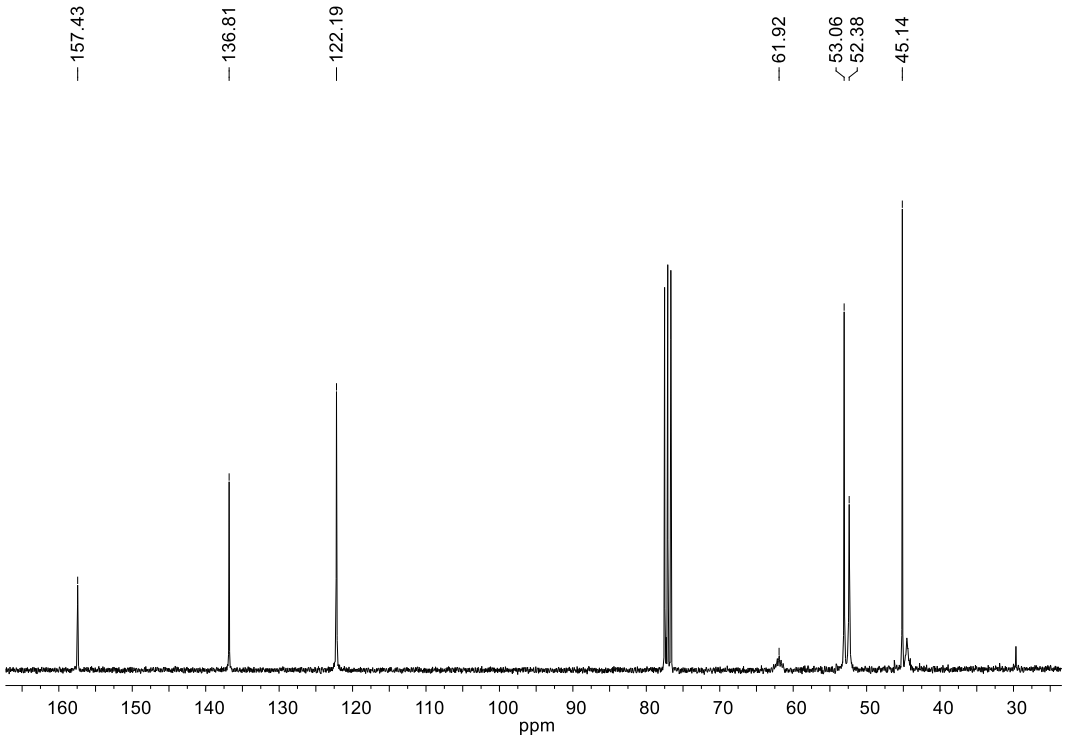

Figure S2. ^{13}C-NMR spectrum of **d_4-PyNMe$_3$** in $CDCl_3$ at 298 K (400 MHz).

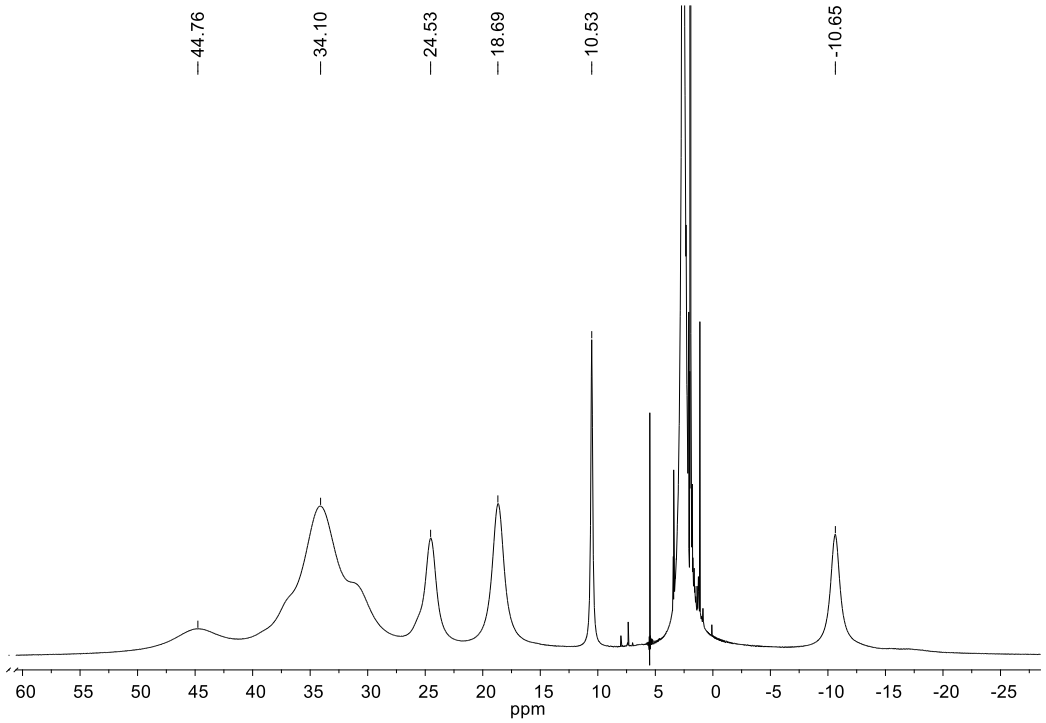

Figure S3. ^{1}H-NMR spectrum of [$Fe^{II}(CF_3SO_3)_2(d_4\text{-PyNMe}_3)$] (**$d_4$-1•$CF_3SO_3$**) in CD_3CN at 243 K (400 MHz).

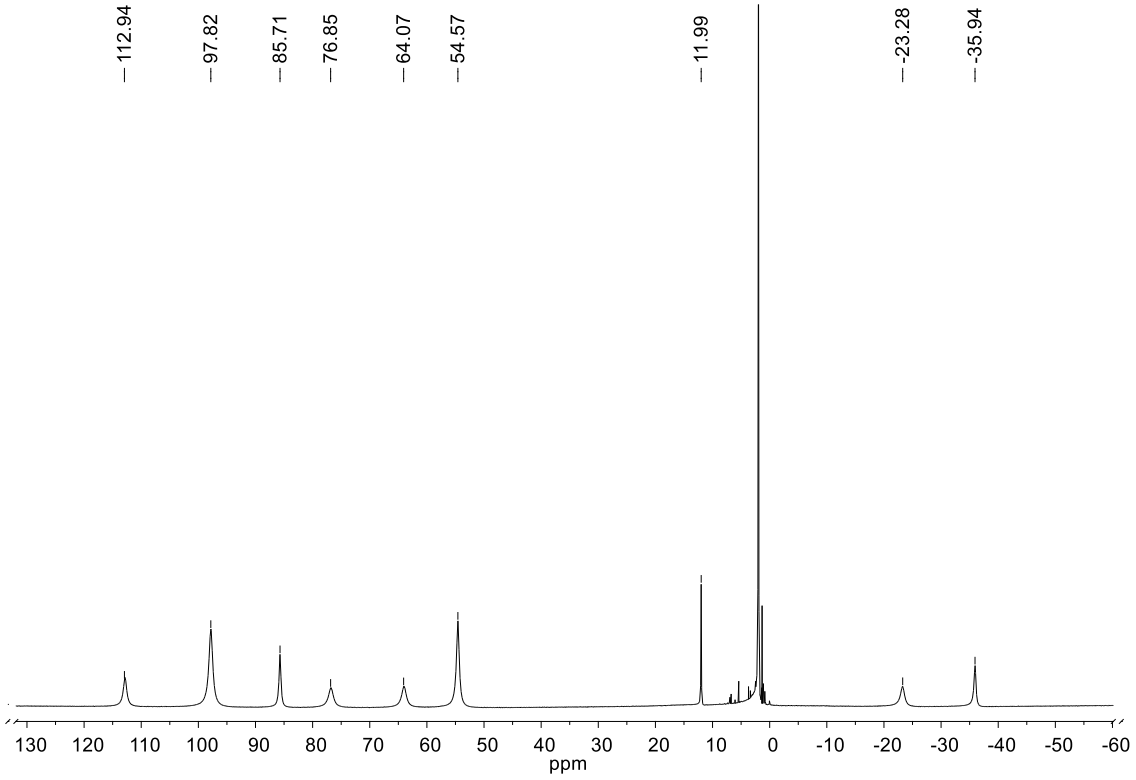

Figure S4. ^{1}H-NMR spectrum of [$Fe^{II}(PyNMe_3)(CH_3CN)_2$]($SbF_6$)$_2$ (**1•SbF_6**) in CD_3CN at 298 K (400 MHz).

Crystal structure determination for 1•SbF_6

Brown crystals of **$C_{18}H_{30}FeN_6F_{12}Sb_2$** were grown from slow diffusion of diethyl ether in a CH_2Cl_2/CH_3CN solution of the compound, and used for low temperature (100(2) K) X-ray structure determination. The measurement was carried out on a *BRUKER SMART APEX CCD* diffractometer using graphite-monochromated Mo *K*α radiation (λ = 0.71073 Å) from an X-ray tube. The measurements were made in the range 2.080 to 28.087° for θ. Full-sphere data collection was carried out with ω and φ scans. A total of 42613 reflections were collected of which 6704 [R(int) = 0.0380] were unique. Programs used: data collection, Smart;[1] data reduction, Saint+;[2] absorption correction, SADABS.[3] Structure solution and refinement was done using SHELXTL.[4]

The structure was solved by direct methods and refined by full-matrix least-squares methods on F^2. The non-hydrogen atoms were refined anisotropically. The H-atoms were placed in geometrically optimized positions and forced to ride on the atom to which they are attached. The data was treated with the TWINROTMAT option of PLATON[5] to find a twin law in which the structure was refined as a two twin component. Twin law: 0 0 -1 0 -1 0 -1 0 0

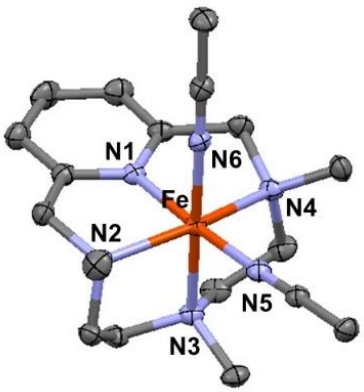

Figure S5. Thermal ellipsoid plot (50% probability) of [$Fe^{II}(PyNMe_3)(CH_3CN)_2$]($SbF_6$)$_2$ (**1•SbF_6**). Hexafluoroantimoniate anions and hydrogen atoms have been omitted for clarity.

Table S1. Crystal data for $[Fe^{II}(PyNMe_3)(CH_3CN)_2](SbF_6)_2$ (**1•SbF$_6$**).

Empirical formula	$C_{18}H_{30}F_{12}FeN_6Sb_2$
Formula weight	857.83
Temperature	100(2) K
Wavelength	0.71073 Å
Crystal system, space group	Monoclinic, P 21/n
Unit cell dimensions	a = 19.573(3) Å α = 90º
	b = 8.2260(11) Å β = 117.913(2)º
	c = 19.595(3) Å γ = 90º
Volume	2787.9(6) A^3
Z, Calculated density	4, 2.044 Mg/m^3
Absorption coefficient	2.538 mm^{-1}
F(000)	1664
Crystal size	0.28 x 0.28 x 0.28 mm
θ range for data collection	2.080 to 28.087º
Limiting indices	-25<=h<=25, -10<=k<=10, -25<=l<=25
Reflections collected / unique	42613 / 6704 [R(int) = 0.0380]
Completeness to θ = 25.242	99.8 %
Absorption correction	Empirical
Max. and min. transmission	1.0 and 0.802306
Refinement method	Full-matrix least-squares on F^2
Data / restraints / parameters	6704 / 0 / 358
Goodness-of-fit on F^2	1.043
Final R indices [I>2σ(I)]	R1 = 0.0268, wR2 = 0.0711
R indices (all data)	R1 = 0.0280, wR2 = 0.0720
Extinction coefficient	n/a
Largest diff. peak and hole	1.742 and -0.695 $e.A^{-3}$

Table S2. Selected bond lengths (Å) and angles (º) for $[Fe^{II}(PyNMe_3)(CH_3CN)_2](SbF_6)_2$ (**1•SbF$_6$**).

Fe(1)-N(1)	1.905(3)	N(5)-Fe(1)-N(3)	91.82(11)
Fe(1)-N(3)	2.049(3)	N(1)-Fe(1)-N(2)	82.62(12)
Fe(1)-N(2)	2.066(3)	N(5)-Fe(1)-N(2)	97.90(11)
Fe(1)-N(4)	2.076(3)	N(6)-Fe(1)-N(2)	95.23(11)
		N(3)-Fe(1)-N(2)	85.55(11)
		N(1)-Fe(1)-N(4)	82.47(12)
N(1)-Fe(1)-N(6)	86.22(11)	N(5)-Fe(1)-N(4)	97.80(12)
N(5)-Fe(1)-N(6)	88.91(12)	N(6)-Fe(1)-N(4)	93.65(11)
N(1)-Fe(1)-N(3)	93.04(11)	N(3)-Fe(1)-N(4)	85.37(11)

2. XAS and Mössbauer analysis for 2a and 2b

2.1 XAS analysis

Table S3. Summary of XAS analysis results for **2a** and **2b**.

Species	K-edge energy (eV)	Pre-edge energy (eV)	Pre-edge area (units)	EXAFS analysis		
				N path	r (Å)	σ^2 (x10^{-3})
2a	7124.8	7114.1	20.9	1 N/O	1.66	1.7
				5 N/O	2.00	7.0
				6 C	2.9	1.7
				3 C	3.04	3.2
2b	7124.4	7114.0	19.6	0.8 N/O	1.65	2.9
				5 N/O	2.00	6.0
				5 C	2.84	3.0
				4 C	2.96	1.7

2.2 Mössbauer analysis

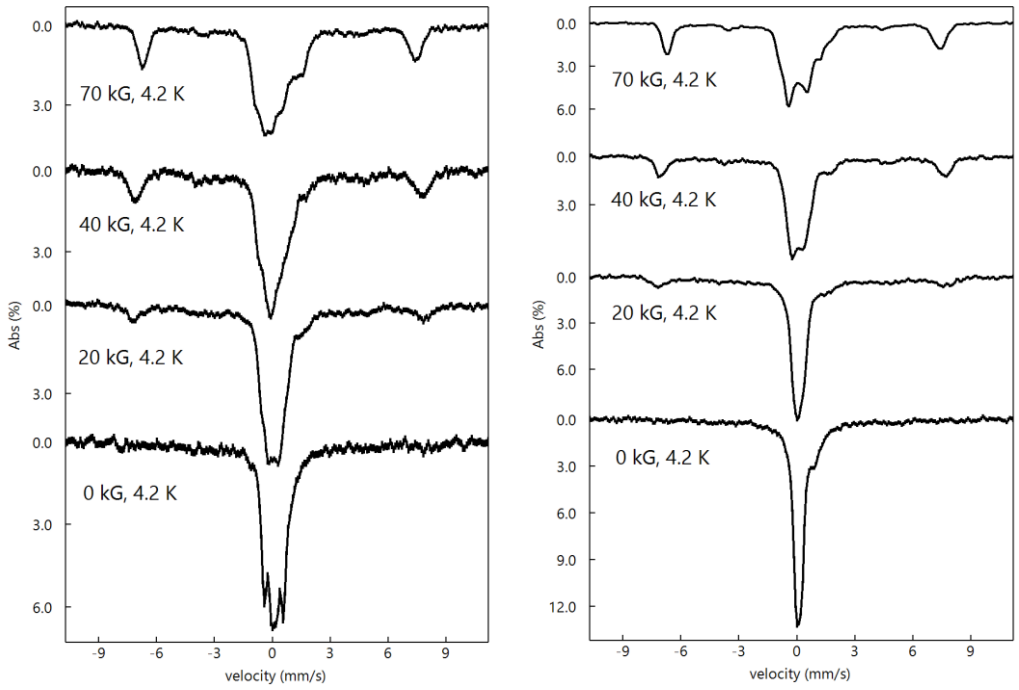

Figure S6. Raw Mössbauer spectra of the samples that mainly contain **2a** (left) or **2b** (right), respectively. Due to the persistent decay species **2a**, the sample on which we collected the spectrum on the left contains almost equal amount of species **2b**.

Techniques applied for obtaining “pure” spectra of **2a** and **2b** from the raw spectra: at first, we started from the right panel in Figure S6 as there are only two species existing in this spectra. By masking the middle doublets, we can use a typical high-spin ferric parameter set ($A/g_n\beta_n$ = (-21, -21, -21)T, δ=0.45 mm/s, ΔE_q =-0.90m/s, η=0.3) to simulate the rest of the spectra at various external fields. By removing the high-spin species with the simulated trace, we can obtain the pure spectrum of **2b** shown in Figure 2. Secondly, the left panel in Figure S6 contains three species: **2a**, **2b** and high-spin ferric. We remove the high-spin ferric with the same technique explained above, and then we estimated the percentages of species **2a** and **2b** from the zero-field doublets. Using the simulation parameters of **2b** obtained above, we can subtract the portion of **2b** from the spectra with various external fields and obtain a “pure” spectrum of **2a** (shown in Figure 2).

3. NMR characterization of 2b and d_4-2b

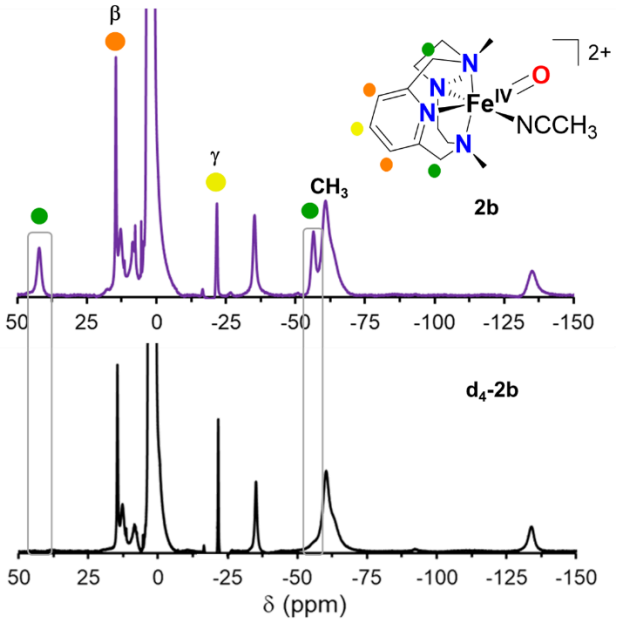

Figure S7. ^{1}H-NMR spectra of **2b** and **d_4-2b** in CD_3CN at -40 ºC. Peak assignments are as follows: benzylic protons at 42 ppm (2H) and -56 ppm (2H); aliphatic CH_2 at 12.9 (2H), 8.5 ppm (2H), -35 ppm (2H) and -133 ppm (2H); CH_3 at -60 ppm (9H); pyridine β at 15 ppm (2H) and pyridine γ at -22 ppm (1H).

4. Conversion of 2a to 2b and comparison of reactivity

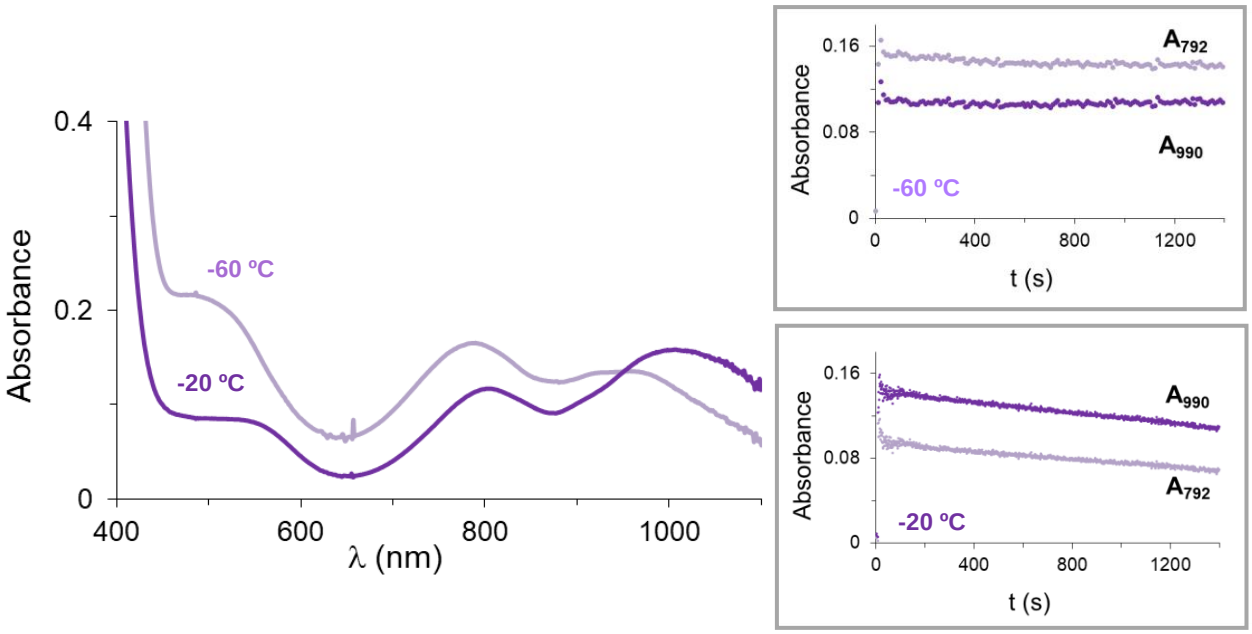

Figure S8. Left: UV-vis absorption spectra of **2** obtained upon reaction of a solution of **1** (1 mM) in CH_3CN:CH_2Cl_2 1:1 with 1.1 equiv Bu_4NIO_4 and 0.8 equiv TfOH at -60 ºC (**2a**+**2b**, light purple line) or -20 ºC (**2b**, dark purple line). Right: kinetic traces at 792 and 990 nm for the reaction at -60 ºC (top) and -20 ºC (bottom).

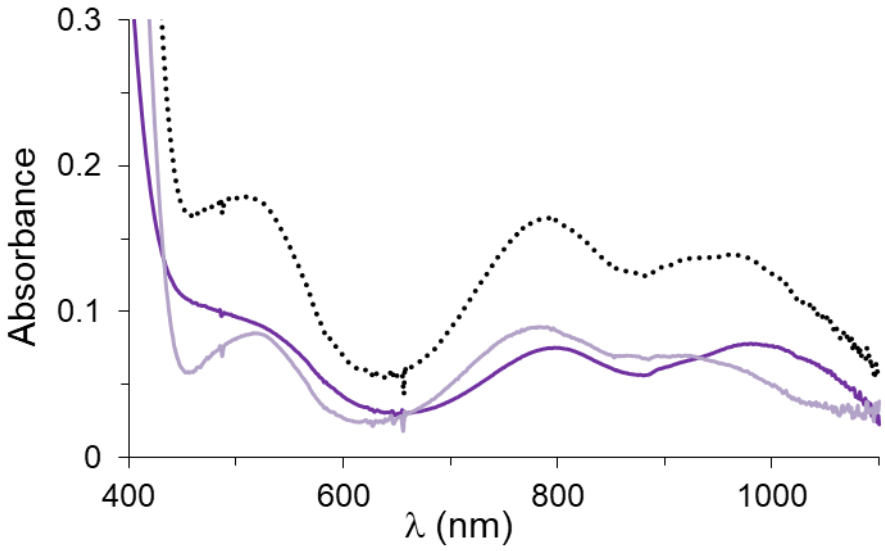

Figure S9. UV-vis absorption spectra of **2a**+**2b** (dashed black line) generated at -60 ºC upon reaction of a solution of **1** (1 mM) in CH_3CN:CH_2Cl_2 1:1 with 1.1 equiv Bu_4NIO_4 and 0.8 equiv TfOH. According to spectroscopic data, this spectrum corresponds to an approximately 1:1 mixture of **2a** and **2b**. The deconvoluted spectrum of **2a** (light purple line) has been obtained by subtracting the contribution of **2b** (dark purple line). The contribution of **2b** corresponds to its UV-vis spectrum at -60 ºC which has been divided by two to get the concentration of **2b** in the mixture.

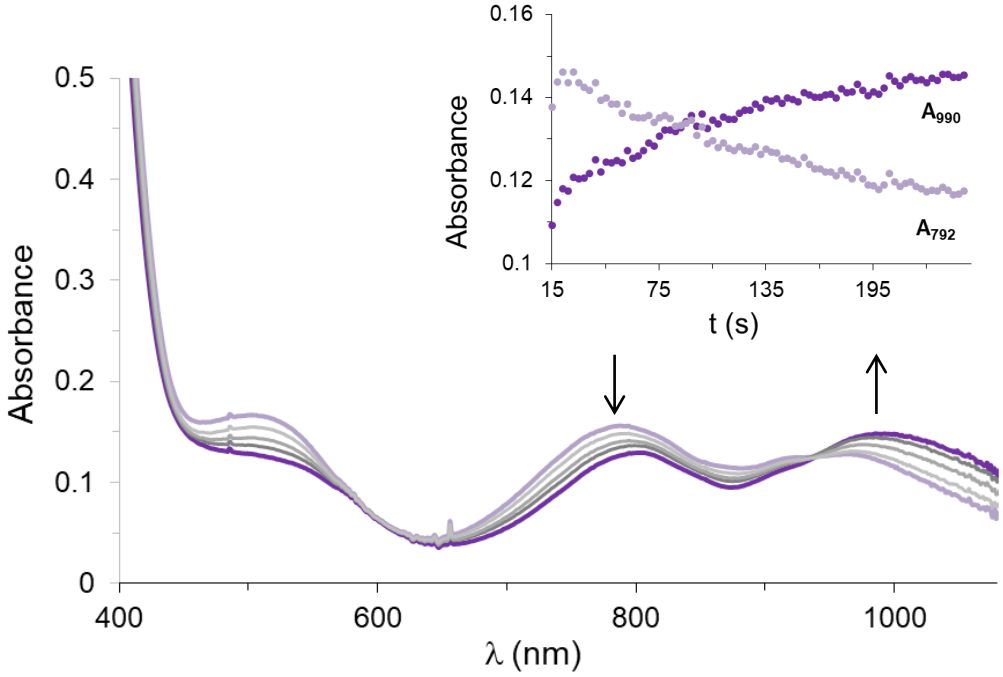

Figure S10. Spectral changes upon reaction of a solution of **1•SbF$_6$** (1 mM) in CH_3CN with 1.1 equiv Bu_4NIO_4 and 0.8 equiv TfOH at -40 ºC (light purple: initial spectra; dark purple: final spectra). Inset: kinetic traces at 792 and 990 nm.

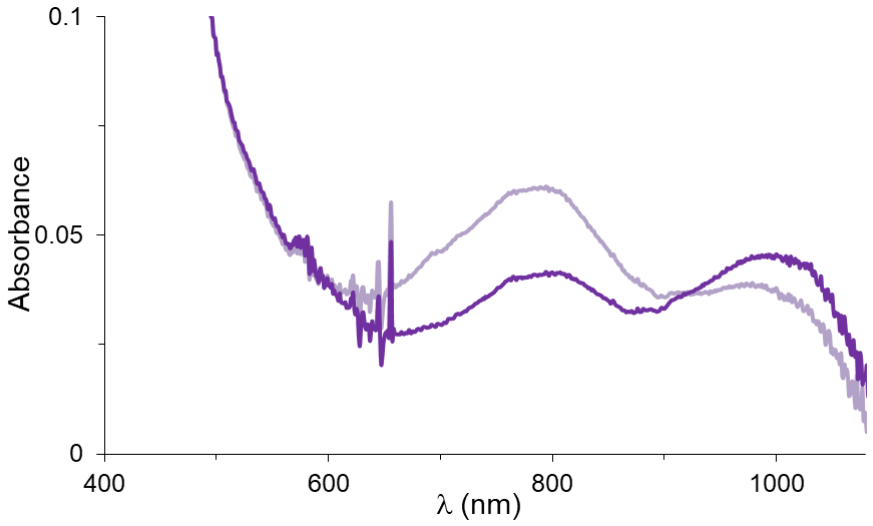

Figure S11. UV-vis absorption spectra of **2** upon reaction of a solution of **1** (1 mM) in CH_3CN with 1.1 equiv 2-*t*$BuSO_2$-C_6H_4IO at -40 ºC (light purple: initial spectra; dark purple: final spectra).

4.1 Reactivity of 2a and 2b

According to spectroscopic data isomer **2a** is always obtained in an approximately equimolar mixture with **2b**. Instead, compound **2b** can be obtained without contamination of **2a** at -40 ºC after isomerization. As a consequence, while the decay of **2b** upon reaction with a substrate can be fitted to a single exponential function ($f = y_0 + a*e^{(-b*x)}$), the decay of **2a** has to be fitted to a double exponential function ($f = y_0 + a*e^{(-b*x)} + c*e^{(-d*x)}$), due to the contamination by **2b**. In this case, the experimental k_{obs} value for the reaction of **2b** with substrates can be fixed to finally get the k_{obs} value for the reaction of **2a**. Alternatively, the contribution of **2b** to the decay of the 792 nm band of **2a** can be subtracted and the resulting data can be fitted to a single exponential function that corresponds to the decay of "pure" **2a**.

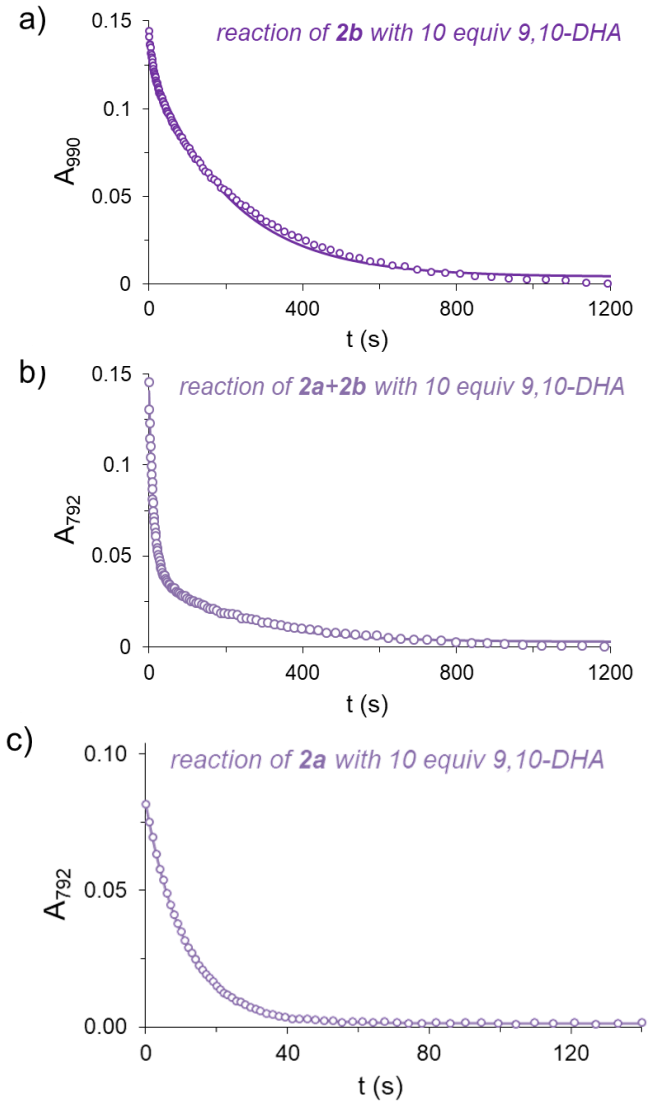

Figure S12. a) Kinetic trace at 990 nm for the reaction of **2b** with 10 equiv 9,10-dihydroanthracene in CH_3CN:CH_2Cl_2 1:1 at -60 ºC (empty circles) and its fitting to a single exponential function (solid line). b) Kinetic trace at 792 nm for the reaction of an approximately 1:1 mixture of **2a**:**2b** with 10 equiv 9,10-dihydroanthracene in CH_3CN:CH_2Cl_2 1:1 at -60 ºC (empty circles) and its fitting to a double exponential function (solid line). c) Kinetic trace at 792 nm for the reaction of **2a** with 10 equiv 9,10-dihydroanthracene in CH_3CN:CH_2Cl_2 1:1 at -60 ºC obtained after subtracting the contribution of **2b** in Figure S12b (empty circles) and its fitting to a single exponential function (solid line).

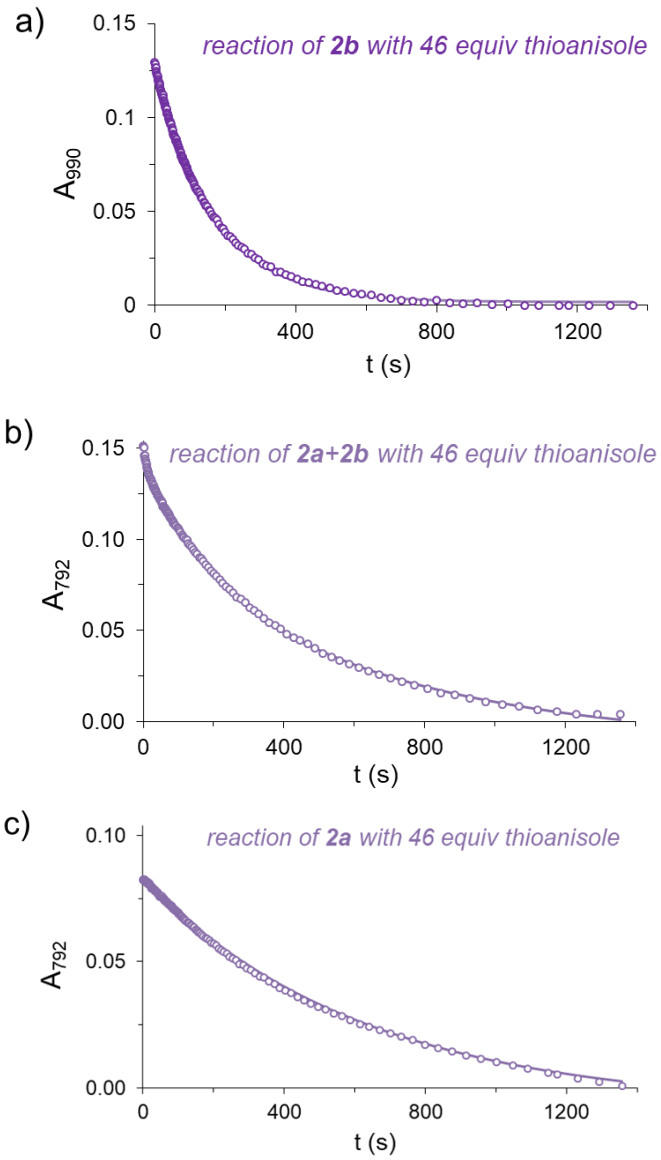

Figure S13. a) Kinetic trace at 990 nm for the reaction of **2b** with 46 equiv thioanisole in CH_3CN:CH_2Cl_2 1:1 at -60 ºC (empty circles) and its fitting to a single exponential function (solid line). b) Kinetic trace at 792 nm for the reaction of an approximately 1:1 mixture of **2a**:**2b** with 46 equiv thioanisole in CH_3CN:CH_2Cl_2 1:1 at -60 ºC (empty circles) and its fitting to a double exponential function (solid line). c) Kinetic trace at 792 nm for the reaction of **2a** with 46 equiv of thioanisole in CH_3CN:CH_2Cl_2 1:1 at -60 ºC obtained after subtracting the contribution of **2b** in Figure S13b (empty circles) and its fitting to a single exponential function (solid line).

5. Reactivity of 2b

5.1 Oxygen atom transfer reactions

Under conditions of excess substrate, the decay of the absorption band of **2b** at 990 nm could be fitted to a single exponential function (Figure S14) indicating a pseudo-first order behavior from which the corresponding k_{obs} values could be extracted. The second order rate constants (k_x) could be calculated affording a value of 0.88 $M^{-1}s^{-1}$ for the reaction with thioanisole. A plot of the logarithm of the reaction rates ratio (k_X/k_H) as a function of the corresponding Hammett parameter (σ_p) gave a good linear correlation with a negative slope (ρ = -1.77), indicating the electrophilic character of **2b** (Figure S15). The Hammett value (ρ) obtained for **2b** is in line with the ones previously reported for the sulfide oxidation carried out by well-defined oxoiron(IV) complexes. For example, Hammett values of -1.4 (at 0 ºC) and -1.5 (at -20 ºC) were described for the oxoiron(IV) complexes bearing pentadentate ligands N4Py and Bn-TPEN, respectively.[6] Similar values were obtained for oxoiron(IV) species with tetradentate ligands such as TPA (ρ = -1.6 at -45 ºC)[6] or Pytacn (ρ= -1.5 at 0 ºC).[7] [TPA = tris(pyridyl-2-methyl)amine; Pytacn = 1,4-dimethyl-7-(2-pyridylmethyl)-1,4,7-triazacyclononane].

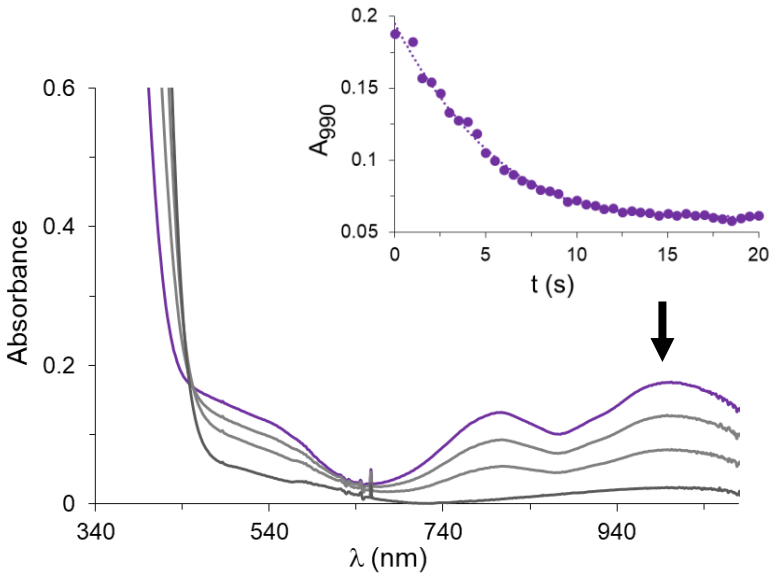

Figure S14. Decay of **2b** upon reaction with 50 equiv of methyl *p*-tolyl sulfide at -40 ºC in CH_3CN. Inset: kinetic trace at 990 nm.

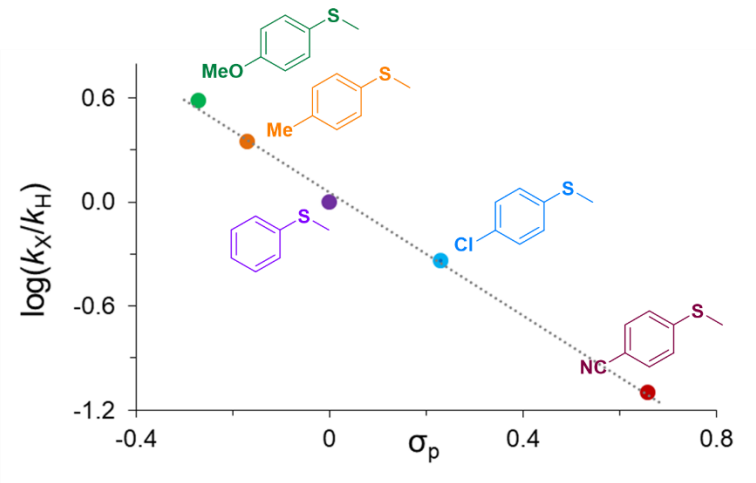

Figure S15. Hammett plot for the reaction of **2b** with *p*-X thioanisoles at -40 ºC in CH_3CN.

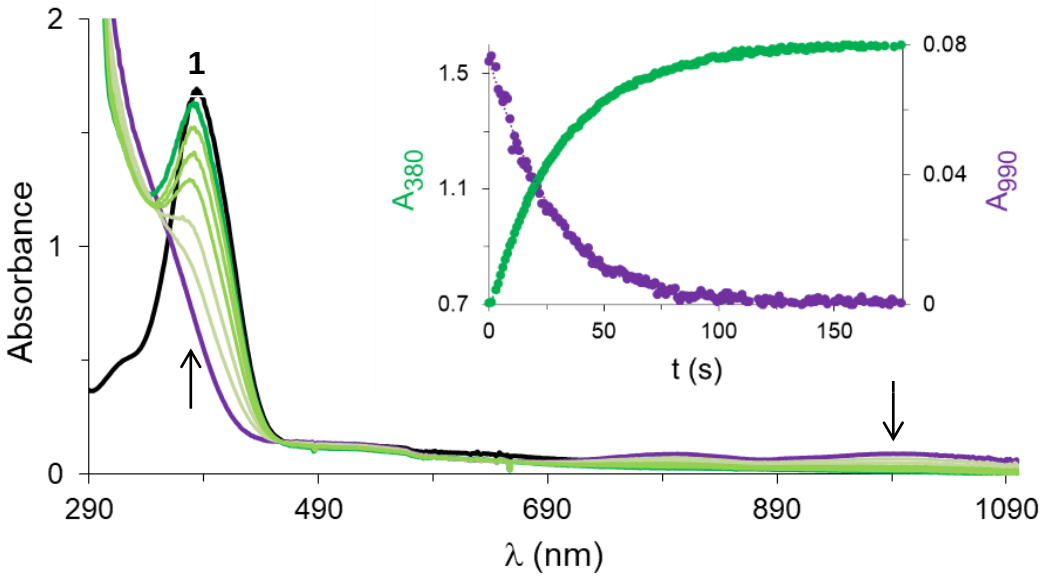

Figure S16. Recovery of **1** (green line) upon reaction of **2b** (dark purple line) with 62 equiv of thioanisole at -40 ºC in CH_3CN. The black line shows the initial spectrum of **1** before **2b** generation. [**1**] = 0.5 mM.

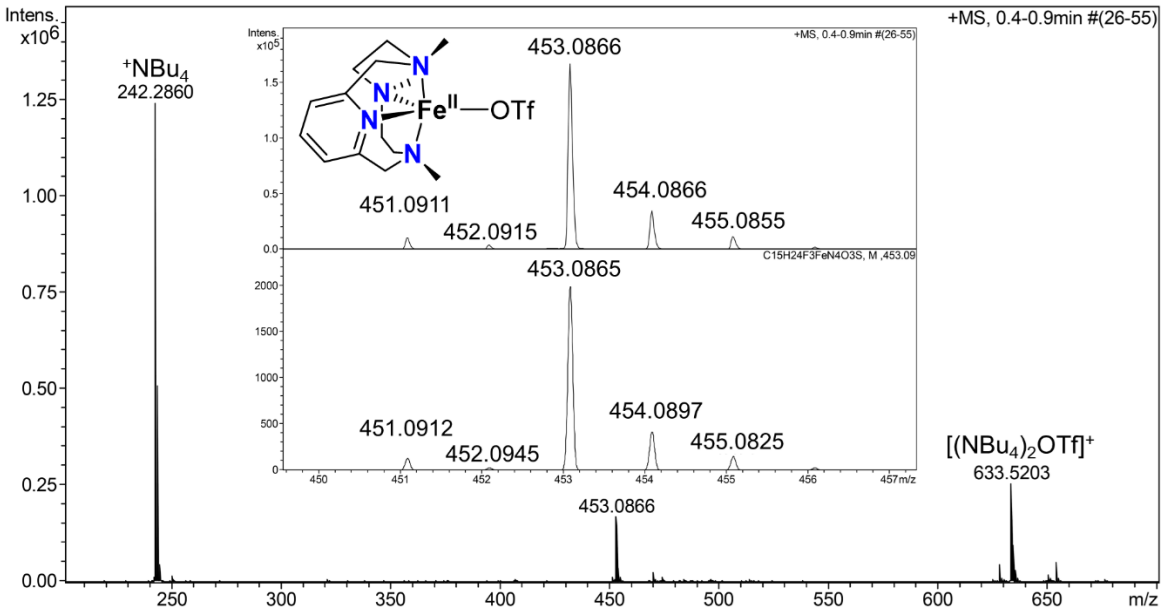

Figure S17. High resolution mass spectrum of the solution obtained after reaction of **2b** with 50 equiv methyl *p*-tolyl sulfide at -40 ºC in CH_3CN. The spectrum was recorded at room temperature.

5.2 Hydrogen atom transfer reactions

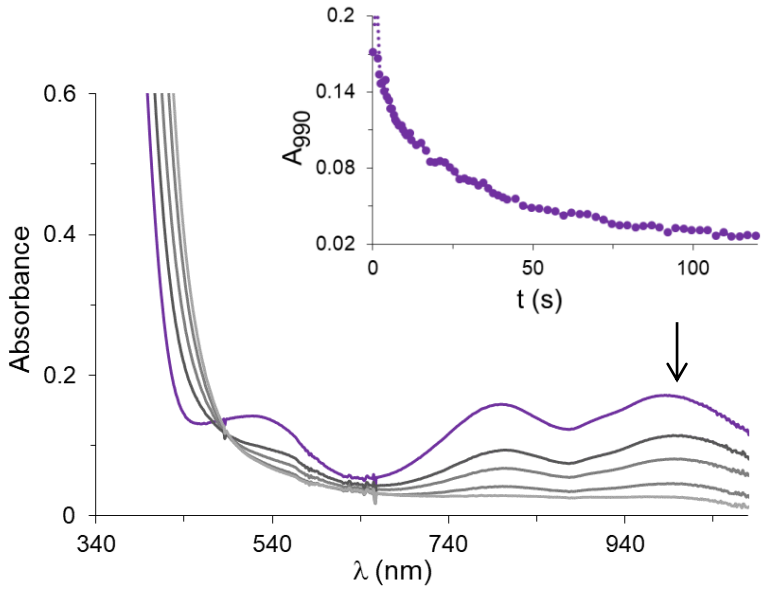

Figure S18. Decay of **2b** upon reaction with 48 equivalents of 9,10-dihydroanthracene in CH_3CN:CH_2Cl_2 1:1 at -40 ºC. Inset: kinetic trace at 990 nm.

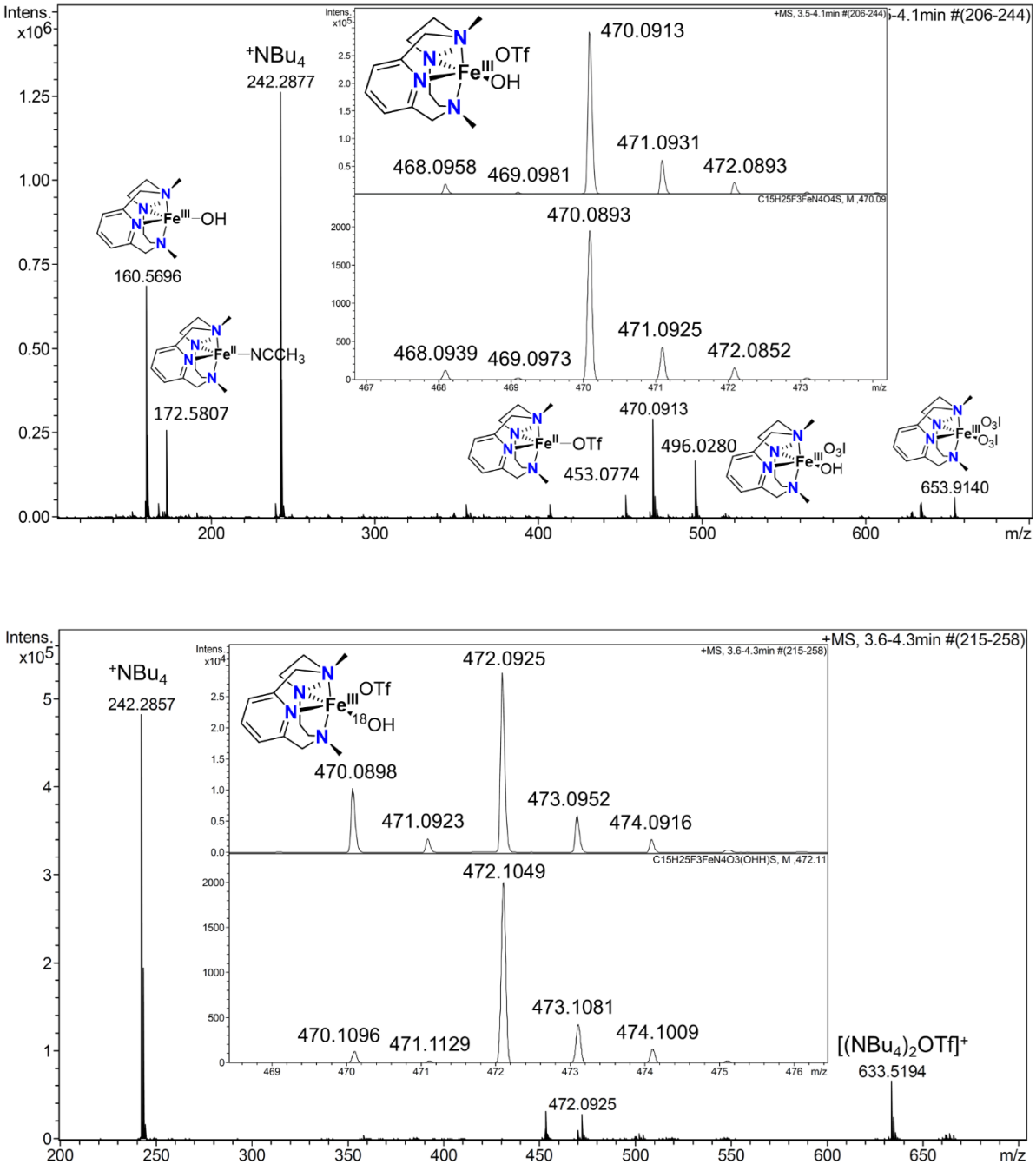

Figure S19. High resolution mass spectrum of the solution obtained after reaction of **2b** with 50 equiv 9,10-dihydroanthracene at -40 ºC in CH_3CN (top). The spectrum was recorded at room temperature. Addition of $H_2{}^{18}O$ to the solution caused a shift of 2 mass/charge units of the peak corresponding to $[Fe^{III}(OH)(CF_3SO_3)(PyNMe_3)]^+$ (bottom).

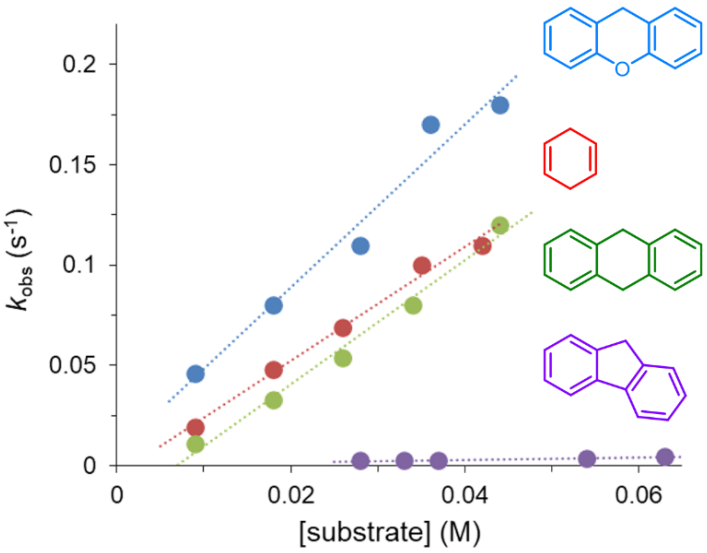

Figure S20. Plot of k_{obs} versus substrate concentration for the reaction of **2b** with different substrates in CH_3CN:CH_2Cl_2 1:1 at -40 ºC.

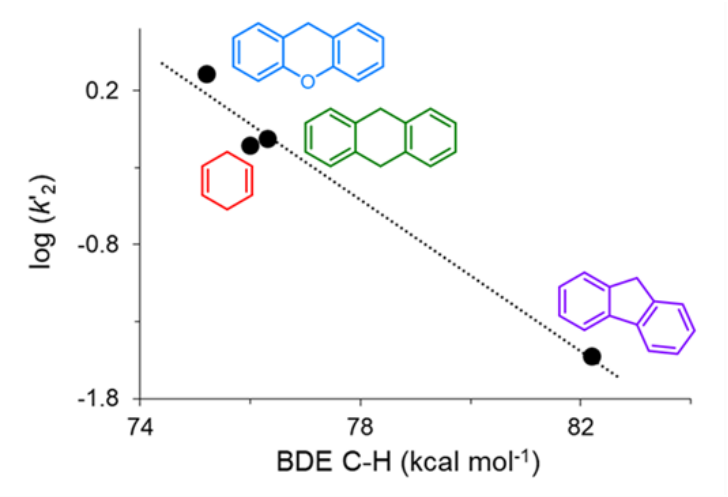

Figure S21. Plot of log(k'_2) versus C−H BDEs for the reaction of **2b** with different substrates in CH_3CN:CH_2Cl_2 1:1 at -40 ºC.

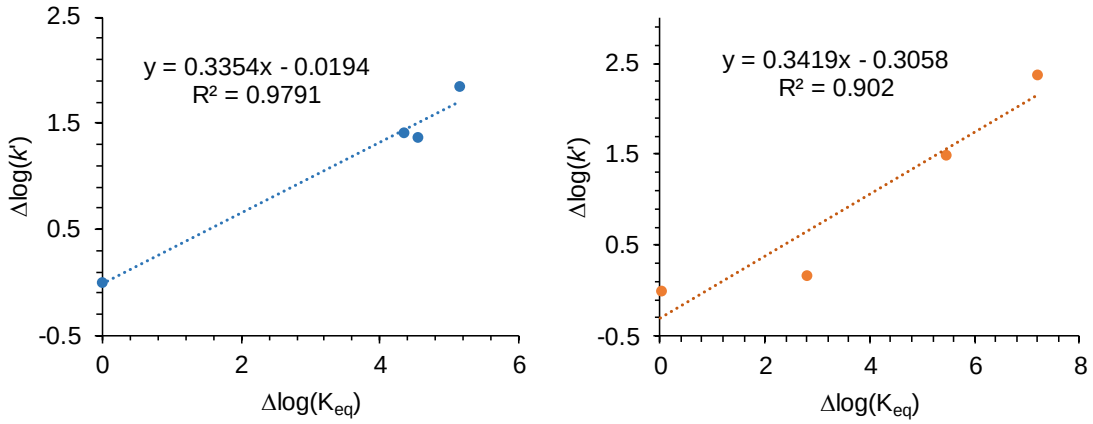

Figure S22. Linear free energy relationship for the reaction of **2b** (left) and **3** (right) with C–H bonds. A unitless slope of 0.34 is obtained in both cases. Log(*k'*) corresponds to the logarithm of the normalized second-order rate constant for the reaction of **2b** or **3** with a given substrate. $\Delta\log(K_{eq})$ is directly related to the BDE of the C–H bond by considering basic thermodynamics ($\Delta G° = -RT\ln K_{eq}$) and assuming that $\Delta(\Delta G°) = \Delta BDE$. T = 298 K.

5.3 Kinetic isotope effect

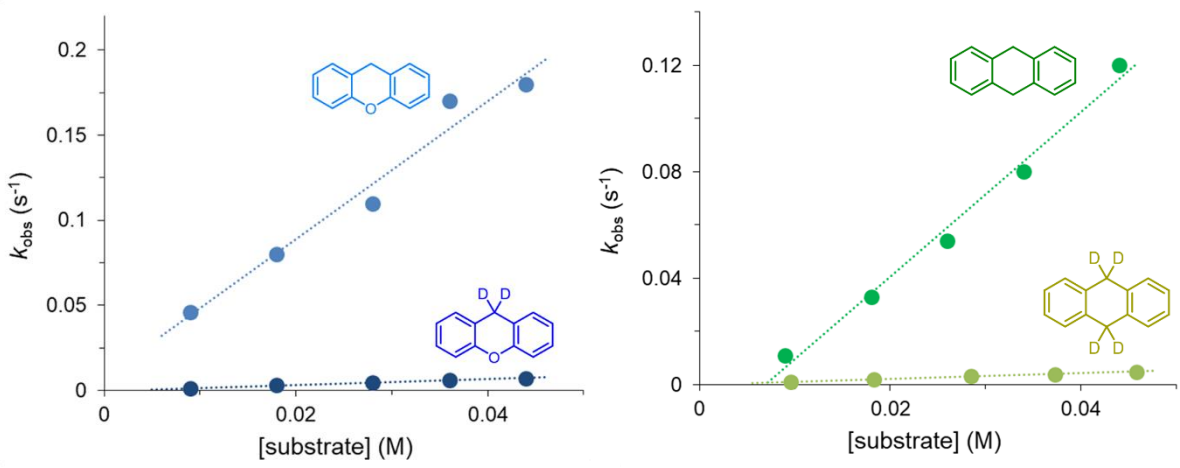

Figure S23. Left: plot of k_{obs} versus substrate concentration for the reaction of **2b** with xanthene and d_2-xanthene in CH_3CN:CH_2Cl_2 1:1 at -40 ºC. Right: plot of k_{obs} versus substrate concentration for the reaction of **2b** with 9,10-dihydroanthracene and d_4-9,10-dihydroanthracene in CH_3CN:CH_2Cl_2 1:1 at -40 ºC.

5.4 Eyring analysis

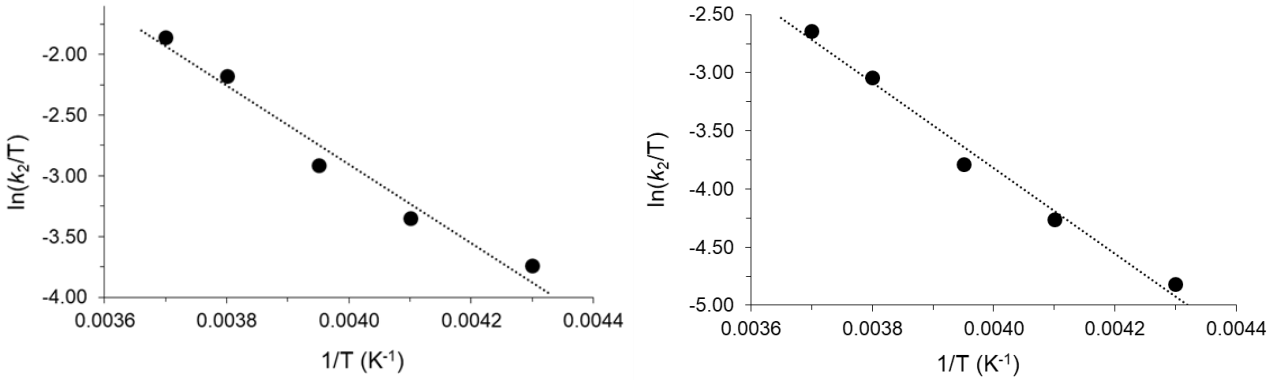

Figure S24. Left: Eyring plot for the reaction of **2b** with xanthene in $CH_3CN:CH_2Cl_2$ 1:1. Right: Eyring plot for the reaction of **2b** with cyclohexadiene in $CH_3CN:CH_2Cl_2$ 1:1.

6. Reaction of 2b and 3 with cyclohexene and cyclohexane

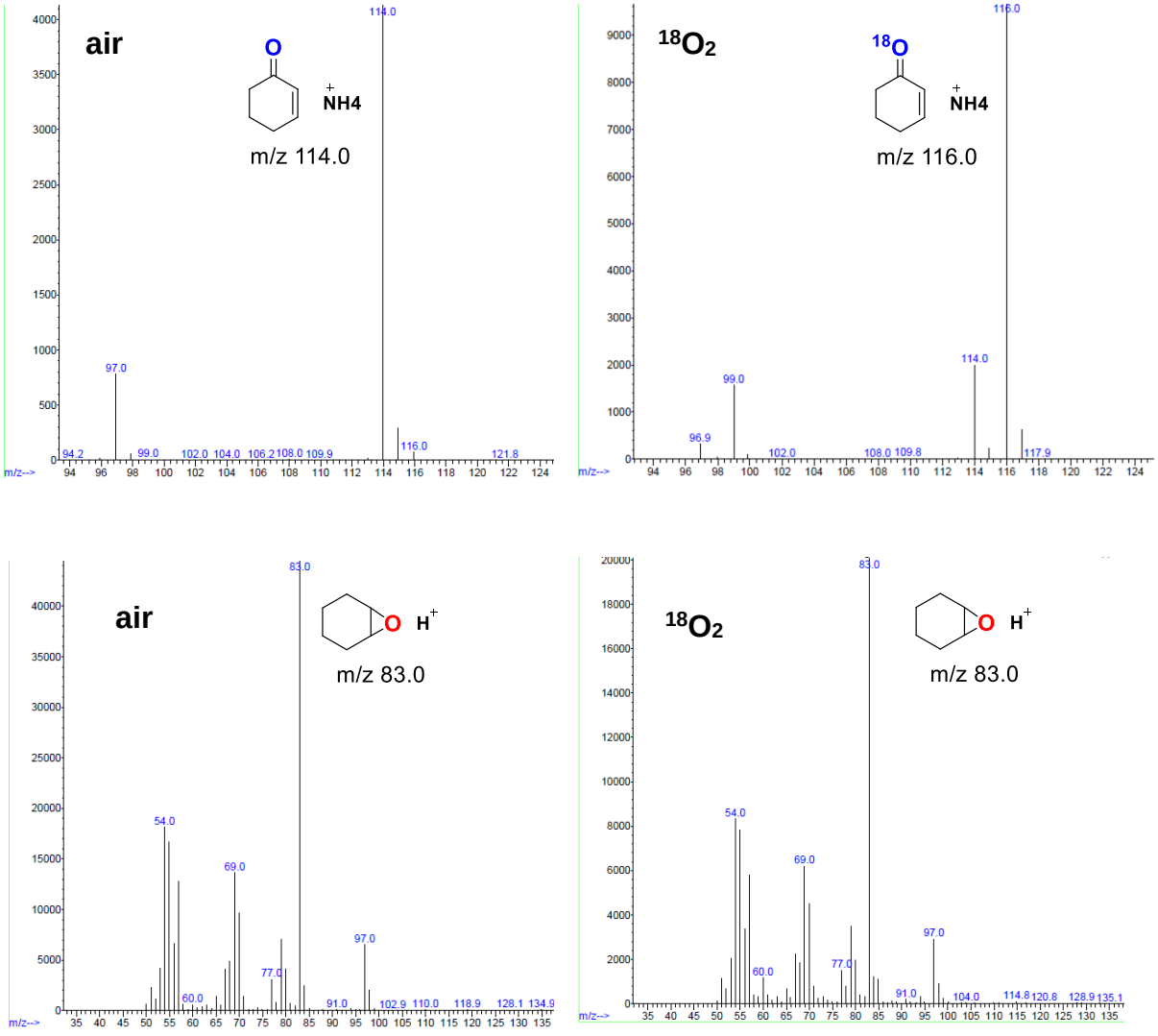

Figure S25. Top: GC-MS spectra (chemical ionization) of the ketone product obtained after reaction of **2b**, in CH_3CN at -40 ºC, with 100 equiv cyclohexene under air (left) or $^{18}O_2$ atmosphere (right). Bottom: GC-MS spectra (electron ionization) of the epoxide product obtained after reaction of **3** with 100 equiv cyclohexene under air (left) or $^{18}O_2$ atmosphere (right).

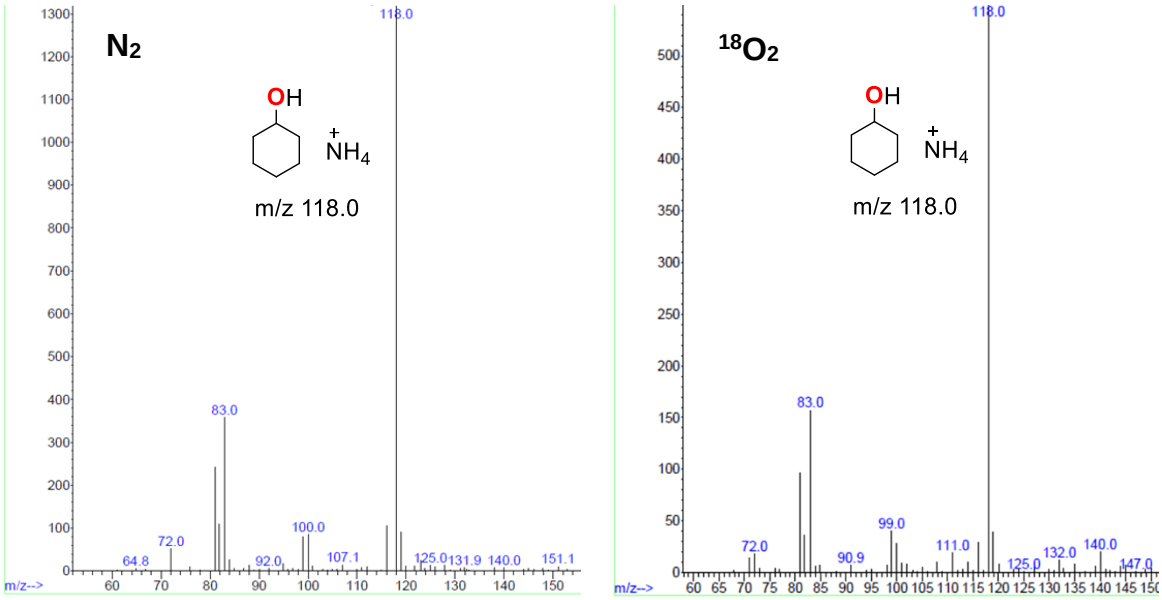

Figure S26. GC-MS spectra (chemical ionization) of cyclohexanol obtained after reaction of **3**, in CH_3CN at -40 ºC, with 45 equiv cyclohexane under N_2 (left) or $^{18}O_2$ atmosphere (right).

7. DFT calculation of species 2a and 2b

We optimized the structures of complexes **2a** and **2b** in Gaussian 16 (Rev. B01)[8] with fine-tuned B3LYP (labeled as B3LYP* in the following) functionals (Iop(3/76=1000001500) Iop(3/77=0720008000) Iop(3/78=0810010000)), a def2tzvp basis set and a built-in acetonitrile solvation model (scrf=(solvent=acetonitrile)). Then we performed ^{1}H-NMR shift calculations by using the same functional but with a Dunning correlation-consistency basis set cc-pVTZ.

The calculations were carried out by following the protocols described by Bagno and coworkers. [9-12] [9-12] [9-12] [9-12] [9-12] [9-12] Geometries were optimized starting from modified XRD structure of **1** by removing counter-ions and adding oxygen.

The calculated ^{1}H-NMR shifts were determined by the following formula:[13,14]

$$\sigma = \sigma_{ref} - (\sigma_{orb} + \sigma_{FC} + \sigma_{PC})$$

where σ_{ref} = 31.02 ppm for TMS was obtained at the same theoretical level as those for the Fe(IV) complexes included in this study. σ_{orb} is the orbital contribution to the proton, which is equivalent to the shielding for diamagnetic systems. The Fermi contact term, σ_{FC}, which originates from the scalar interaction between magnetic field from unpaired electrons and the magnetic momentum of target proton, dominates the paramagnetic component in the ^{1}H-NMR shift arising from the paramagnetic center. The Fermi contact term can be calculated from Fermi's hyperfine interaction parameters as the following:

$$\sigma_{FC} = \frac{2\pi}{\gamma_I} g_{iso} \mu_B A \frac{S(S+1)}{3kT}$$

in which γ_I is the magnetogyric ratio of the nucleus I and g_{iso} is the isotropic g factor of the spin system, μ_B is the Bohr magneton and A is the Fermi hyperfine interaction parameter. The contribution from pseudo-contact term σ_{PC}, can be approximated by the theory developed by Hrobárik et al.[15] Usually it is small and can be ignored compared with σ_{FC}. In this work we estimate the ^{1}H-NMR shift only by the orbital term and Fermi-contact term. All calculations were done at 208 K, the same temperature at which the ^{1}H-NMR measurements were performed in this work.

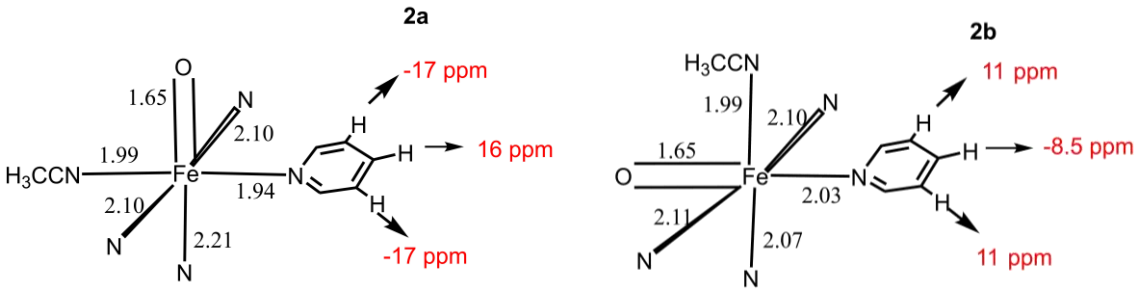

Figure S27. Important bond lengths (black, in Angström) in DFT-optimized geometry structure of **2a** and **2b**; calculated ^{1}H-NMR chemical shifts of β,γ-H's (red).

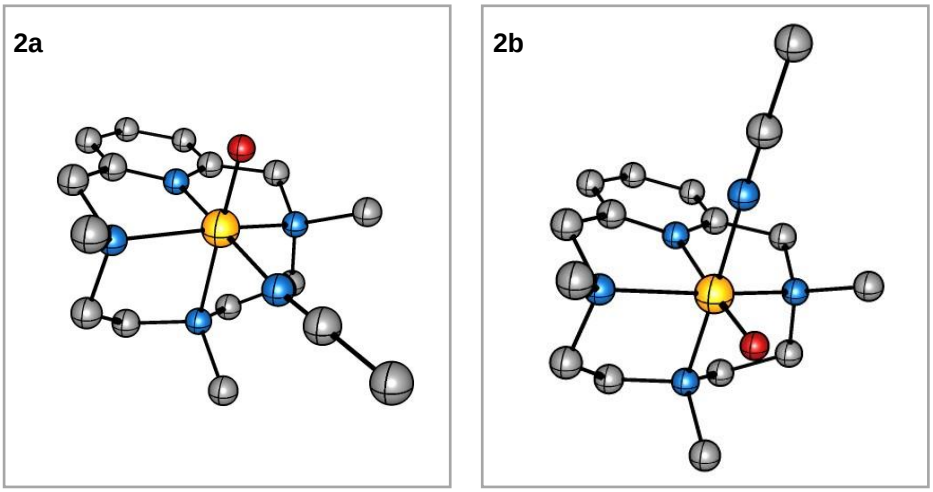

Figure S28. DFT calculated structure of **2a** (left) and **2b** (right).

7.1 Geometry coordinates for 2a and 2b

2a

Fe	0.380569	0.000005	-0.44734
N	0.130219	-2.07027	-0.20333
N	0.537948	0.000159	1.754284
N	0.129978	2.070268	-0.20342
C	-3.62012	-1.22541	-0.29979
H	-4.15004	-2.1886	-0.29925
C	-2.21584	-1.19074	-0.37885
C	-1.30305	-2.37827	-0.6309
H	-1.29148	-2.55959	-1.72673
H	-1.66363	-3.30667	-0.14064
C	1.065125	-2.91988	-1.03699
H	0.819525	-3.99556	-0.90625
H	2.106037	-2.7389	-0.71285
H	0.954531	-2.63276	-2.0993
C	0.3196	-2.41401	1.27663
H	1.399756	-2.59622	1.433802
H	-0.21108	-3.36127	1.510683
C	-0.1728	-1.26679	2.179086
H	-1.26566	-1.11605	2.087849
H	0.039826	-1.50388	3.244564
C	1.923416	0.000433	2.369724
H	1.830599	0.000525	3.47728
H	2.488756	0.894134	2.05241
H	2.488984	-0.89319	2.052589
C	-0.17327	1.266846	2.17905
H	0.039207	1.504037	3.244537
H	-1.26607	1.115728	2.087728

C	0.318816	2.414194	1.276587
H	-0.21238	3.36121	1.510437
H	1.39884	2.596919	1.434043
C	1.065041	2.91992	-1.03685
H	0.954742	2.632785	-2.09918
H	2.105881	2.739009	-0.71244
H	0.819341	3.995595	-0.90619
C	-4.32127	-0.00019	-0.23798
C	-3.6202	1.225089	-0.30009
H	-4.1502	2.188239	-0.2998
C	-1.30318	2.378007	-0.63149
H	-1.66394	3.306604	-0.14174
H	-1.2913	2.558804	-1.72741
N	2.367398	0.000056	-0.51885
C	3.519056	0.000013	-0.72123
C	4.966724	-2.3E-05	-0.96406
H	5.41785	0.905996	-0.51006
H	5.156034	-9.9E-05	-2.05713
H	5.417811	-0.90603	-0.50999
O	0.321902	0.000036	-2.09401
N	-1.55341	-0.0001	-0.36016
C	-2.21595	1.190515	-0.37916
H	-5.41948	-0.00023	-0.16584

2b

Fe	-0.41036	-0.67272	0.037453
N	-0.3208	-0.43185	-2.05276
N	-2.10347	0.510415	-0.04832
N	-0.35795	-0.18725	2.08564
C	2.068365	2.516349	-1.35986
H	2.40676	2.876465	-2.34215
C	1.259644	1.368988	-1.25937
C	0.896407	0.426544	-2.39984
H	1.7561	-0.26062	-2.55038
H	0.727956	0.96004	-3.35852
C	-0.23505	-1.7325	-2.82298
H	-0.22773	-1.52746	-3.91504
H	-1.10805	-2.35788	-2.56133
H	0.692148	-2.26389	-2.54045
C	-1.60354	0.294842	-2.45724
H	-2.38049	-0.47619	-2.61711
H	-1.4539	0.820274	-3.42381
C	-2.02947	1.278099	-1.35607
H	-1.3037	2.105979	-1.242
H	-3.01643	1.728466	-1.59477
C	-3.40546	-0.27524	-0.01828

H	-4.25362	0.439674	-0.07209
H	-3.47006	-0.86845	0.909104
H	-3.44752	-0.97506	-0.86949
C	-2.05817	1.421017	1.165767
H	-3.05109	1.890071	1.332458
H	-1.3324	2.234117	0.973399
C	-1.65209	0.571317	2.379553
H	-1.5255	1.203353	3.283621
H	-2.42911	-0.18203	2.609099
C	-0.2794	-1.38809	3.004125
H	0.653562	-1.94416	2.798719
H	-1.14645	-2.04397	2.805562
H	-0.2883	-1.05615	4.064425
C	2.438862	3.17923	-0.16715
C	2.040073	2.667726	1.089028
H	2.354907	3.147661	2.026798
C	0.848922	0.714768	2.351297
H	0.658711	1.359631	3.234461
H	1.7078	0.056717	2.60204
N	0.825435	0.930934	-0.04664
C	1.234464	1.513641	1.112395
N	1.271369	-1.728	0.113699
C	2.233029	-2.39155	0.159264
C	3.437412	-3.23039	0.207547
H	3.999787	-3.01483	1.138945
H	3.142637	-4.29948	0.191843
H	4.077956	-3.00946	-0.67061
O	-1.31255	-2.0509	0.112365
H	3.059597	4.086811	-0.21587

8. References

(1) Bruker Advanced X-ray Solutions. SMART: Version 5.631, 1997-2002.
(2) Bruker Advanced X-ray Solutions. SAINT +, Version 6.36A, 2001.
(3) G. M. Sheldrick, Empirical Absorption Correction Program, Universität Göttingen, 1996.
(4) M. Sheldrick, Program for Crystal Structure Refinement, Universität Göttingen, 1997. Bruker Advanced X-ray Solutions. SHELXTL Version 1996.1914, 2000-2003. SHELXL-2013 (Sheldrick, 2013).
(5) Spek, A. L. (2005). PLATON, A Multipurpose Crystallographic Tool, Utrecht University, Utrecht, THe Netherlands.
(6) Park, M. J.; Lee, J.; Suh, Y.; Kim, J.; Nam, W. Reactivities of Mononuclear Non-Heme Iron Intermediates Including Evidence that Iron(III)−Hydroperoxo Species Is a Sluggish Oxidant. *J. Am. Chem. Soc.* **2006**, *128*, 2630-2634.
(7) Company, A.; Prat, I.; Frisch, J. R.; Mas-Ballesté, D. R.; Güell, M.; Juhász, G.; Ribas, X.; Münck, D. E.; Luis, J. M.; Que, L.; Costas, M. Modeling the cis-Oxo-Labile Binding Site Motif of Non-Heme Iron Oxygenases: Water Exchange and Oxidation Reactivity of a Non-Heme Iron(IV)-Oxo Compound Bearing a Tripodal Tetradentate Ligand. *Chem. Eur. J.* **2011**, *17*, 1622-1634.
(8) M. J. Frisch, G. W. T., H. B. Schlegel, G. E. Scuseria, M. A. Robb, J. R. Cheeseman, G. Scalmani, V. Barone, G. A. Petersson, H. Nakatsuji, X. Li, M. Caricato, A. V. Marenich, J. Bloino, B. G. Janesko, R. Gomperts, B. Mennucci, H. P. Hratchian, J. V. Ortiz, A. F. Izmaylov, J. L. Sonnenberg, D. Williams-Young, F. Ding, F. Lipparini, F. Egidi, J. Goings, B. Peng, A. Petrone, T. Henderson, D. Ranasinghe, V. G. Zakrzewski, J. Gao, N. Rega, G. Zheng, W. Liang, M. Hada, M. Ehara, K. Toyota, R. Fukuda, J. Hasegawa, M. Ishida, T. Nakajima, Y. Honda, O. Kitao, H. Nakai, T. Vreven, K. Throssell, J. A. Montgomery, Jr., J. E. Peralta, F. Ogliaro, M. J. Bearpark, J. J. Heyd, E. N. Brothers, K. N. Kudin, V. N. Staroverov, T. A. Keith, R. Kobayashi, J. Normand, K. Raghavachari, A. P. Rendell, J. C. Burant, S. S. Iyengar, J. Tomasi, M. Cossi, J. M. Millam, M. Klene, C. Adamo, R. Cammi, J. W. Ochterski, R. L. Martin, K. Morokuma, O. Farkas, J. B. Foresman, and D. J. Fox; Gaussian, Inc., Wallingford CT: 2016.
(9) Borgogno, A.; Rastrelli, F.; Bagno, A. Characterization of Paramagnetic Reactive Intermediates: Predicting the NMR Spectra of Iron(IV)–Oxo Complexes by DFT. *Chem. Eur. J.* **2015**, *21*, 12960-12970.
(10) Borgogno, A.; Rastrelli, F.; Bagno, A. Predicting the spin state of paramagnetic iron complexes by DFT calculation of proton NMR spectra. *Dalton Trans.* **2014**, *43*, 9486-9496.
(11) Rastrelli, F.; Bagno, A. Predicting the 1H and 13C NMR spectra of paramagnetic Ru(III) complexes by DFT. *Magn. Reson. Chem.* **2010**, *48*, S132-S141.
(12) Rastrelli, F.; Bagno, A. Predicting the NMR Spectra of Paramagnetic Molecules by DFT: Application to Organic Free Radicals and Transition-Metal Complexes. *Chem. Eur. J* **2009**, *15*, 7990-8004.
(13) Bertini, I.; Luchinat, C.; Parigi, G. *Solution NMR of Paramagnetic Molecules: Applications to Metallobiomolecules and Models*; 1st ed.; Elsevier, 2001; Vol. 2.
(14) Bertini, I.; Luchinat, C.; Parigi, G. *Reson. Spectrosc.* **2002**, *40*, 249-273.
(15) Hrobárik, P.; Reviakine, R.; Arbuznikov, A. V.; Malkina, O. L.; Malkin, V. G.; Köhler, F. H.; Kaupp, M. *J. Chem. Phys.* **2007,** *126*, 024107.